Structural integrity and characteristics at lattice and nanometre levels of ZrN polycrystalline irradiated by 4 MeV Au ions

Weichao Bao [a,b,d], Stuart Robertson [c], Ji-Xuan Liu [b], Guo-Jun Zhang [b,*] Fangfang Xu [a,*], Houzheng Wu [c,*]

[a] State Key Laboratory of High Performance Ceramics and Superfine Microstructure, Shanghai Institute of Ceramics, Shanghai, 200050, China

[b] State Key Laboratory for Modification of Chemical Fibers and Polymer Materials, Institute of Functional Materials, Donghua University, Shanghai, 201620, China

[c] Department of Materials, Loughborough University, Leicestershire LE11 3TU, United Kingdom

[d] University of Chinese Academy of Sciences, Beijing, 100049, China

*Corresponding Author: gjzhang@dhu.edu.cn, ffxu@mail.sic.ac.cn, H.Wu2@lboro.ac.uk

Abstract

We report an as-hot-pressed zirconium nitride polycrystalline with its primary crystal structure maintained no change but lattice defects and features were introduced at nanometre-scale after being irradiated by 4 MeV Au^{2+} with a total fluence of $5x10^{16}/cm^2$. The variation of grey-level seen in backscattered electron images and electron backscattered diffraction maps directly evidenced the structure integrity of the polycrystalline ZrN is well maintained with no crystal structure change of ZrN. The irradiation depth had no relevance to crystal orientation, and Au deposition peaked at a depth of ~0.58 μm with a near-Gaussian distribution. Within a depth <0.58 μm, long dislocation lines were developed with a Burgers vector of $[01\bar{1}]_b/2$ and density $3.2x10^{14}$ $1/m^2$; beyond this depth, dislocation loops were formed with much higher density. In the irradiation damage processes are discussed based on the observed features.

View metadata, citation and similar papers at core.ac.uk

brought to you by CORE

provided by Loughborough University Institutional Repository

Keywords: ZrN; Radiation damage; Structural integrity

1. Introduction

Nuclear power is deemed as a sustainable and clean energy, one of the possible solutions to reduce the dependence of human beings on fossil fuels in the near future [1]. However, the accumulation of spent nuclear fuel containing long-lived fission products is a growing problem worldwide [2]. To reduce the toxicity of nuclear waste, one concept is to develop inert matrix fuels (IMF) for transmuting transuranium elements for further use as fission fuel and producing clean wastes [3]. Zirconium nitride (ZrN) has been proposed as a ceramic target of IMF, based on its superior properties such as high melting point, high thermal conductivity and excellent solubility for minor actinide (MA: Np, Am, Cm) elements [4, 5], making it possible to directly burn plutonium or transmuting long-lived actinides in an accelerator-driven sub-critical system (ADS) or a fast reactor (FR) [6, 7]. In addition, due to its outstanding properties, ZrN is considered as promising fuel phase in the generation IV Gas-cooled Fast Reactor (GFR) [8]. To fully utilize such inherent properties, ZrN matrix must be inert enough even under high dose neutron irradiation, to sustain its mechanical behaviour.

ZrN has the NaCl crystal structure, consisting of two intercalated face-centred sub-networks. It exhibits a broad range of non-stoichiometry that may affect its electronic structure, vacancy concentration, and hence structure stability during irradiation [9]. However, knowledge on such stability is limited in literatures, apart from a handful of research papers directly relevant to this topic. Yang *et al.* investigated the structure change of ZrN ceramics irradiated by proton with a relatively low dose of 0.35 and 0.75 dpa [10]. They demonstrated that ZrN crystal lattice was stable and irradiation damage appeared through generation of dislocation loops and possible point defects. Gan *et al* also investigated the microstructural response of SiC, ZrC and ZrN irradiated to proton irradiation, evidencing that ZrN crystal was more stable than others [11]. Recently, Egeland *et al* investigated the structure of ZrN irradiated by Xe and Kr heavy-ions up to a dose of 200 dpa at different temperatures [12]. Their results showed that crystal lattice structure was maintained no change apart from the formation of lattice defects, typically

dislocations and N vacancies. Very recently, Ogarkov *et al* and Kuznetsov *et al* [13, 14] investigated the structure of ZrN irradiated by high energy Xe ions (167 MeV) and no lattice damage was seen apart from distortion, whilst no detailed characterization is available on the structure after irradiation.

In this study, we will report the structure integrity of a ZrN polycrystalline material after irradiating by heavy ions of a much higher total fluence, followed by detailed analysis of key structure features that might have been developed during irradiation. The irradiation was accomplished through Au ion implantation at room temperature; structure integrity was examined with techniques based on backscattered electron (BSE) imaging and electron backscattered diffraction (EBSD) mapping; detailed microstructural features and chemical compositions were characterised with transmission electron microscopy (TEM), including selected-area diffraction (SAD), high resolution (HR), bright field (BF), dark field (DF), scanning TEM (STEM) with EDS.

2. Experimental procedures

2.1. Zirconium nitride ceramic manufacture

Table 1 Chemical composition of other chemicals in ZrN powder.

Chemical element	**Hf**	**Na**	**Fe**	**O**
wt%	2.6	0.8	0.3	1

ZrN polycrystalline samples were manufactured by hot-pressing commercial ZrN powder (Beijing Dk Nano Technology Co., Ltd., Beijing, China). The as-purchased powder had a lattice parameter of 4.5783 Å and particle size of 800 nm for D50 and 1000 nm for D90. The ZrN content was 95.3 wt%, and other chemicals in the powder is listed in Table 1, as claimed by the supplier.

The as-purchased ZrN powder was dispersed in ethanol in a polyethylene plastic bottle with silicon nitride spherical balls (~10 mm) included as milling medium. The weight ratio of ZrN to milling medium was 1/2. After sealing, the bottle was set up on a rotating rig for ball milling. The rotating speed of the bottle and ball milling time was set up as 120 rpm and 24 h respectively. After ball milling, the slurry was dried at 60˚C in a

vacuum using a rotary evaporator, and the dried powder was sieved through a 200-mesh screen to eliminate large lumps. The as-treated powder was filled in a graphite die coated with boron nitride. Graphite sheets were set between ZrN powder and punches.

For the densification, key steps are highlighted here. Firstly, the furnace was pumped down to a vacuum with a pressure of ~10 Pa at room temperature; such a vacuum level was maintained till the furnace temperature reached to 1300˚C. The primary purpose of this step is to remove absorbed gases from the powder. Secondly, at 1300˚C, flowing argon was turned on, keeping the furnace pressure same as atmosphere one. Thirdly, pressure was applied to a level of 30 MPa when the furnace temperature reached to 2000˚C, and a dwelling time of 1 hr was set to accomplish the densification by switching off power for cooling down naturally.

The surface layer of all as-manufactured ZrN samples were ground off. Their densities were measured using an Archimedean method, giving an average density of 7.17 g/cm^3, equivalent to 98% of the theoretical density (7.32 g/cm^3). Cuboidal samples with dimensions of ~5 x ~5 x ~5 mm were cut from an as-ground plate. Their surfaces to be irradiated were finished by polishing with diamond slurries by starting from an average grit size of 2.5, then 1 and finally 0.5 μm on a lapping machine (UNIPOL-802, Shenyang Kejing Auto-instrument Co. Ltd., China).

2.2. Au ion irradiation

The Au ion irradiation was accomplished on the PKU Tandem Accelerator (Peking University, China) at room temperature. During irradiation, the chamber was maintained in vacuum with a pressure < 10^{-3} Pa; the ion beam direction was set perpendicular to the surface of irradiated surface. The energy of the ion beam was 4 MeV, and an accumulated ion fluence of $5x10^{16}/cm^2$ was implanted on the surface of each irradiated sample.

2.3. Characterization

(a) sample preparation

Samples with as-polished and as-irradiated surfaces were sectioned perpendicular to the surfaces with a diamond cut-off wheel (Pace Technologies, Arizona, USA) using an

Accutom-5 (Struers, Cleveland, USA). The sectioned samples were left and mounted in resin for X-ray diffraction (XRD) and focused ion beam microscopy (FIB), and those for cross-section examination by scanning electron microscopy (SEM) was mounted in conductive Bakelite. The samples were polished using a Labopol-30 with Labopress-100 (Struers, Cleveland, USA) auto loading and dosing system. Grinding from 220-1200 grit was conducted followed by polishing with Struers diamond suspensions with grit size from 9 to 1 μm. A final colloidal silica (Buehler, Illinois, USA) polishing step was used to prepare the sample for EBSD study.

TEM samples were prepared through two routes: (i) Ar ion milling, and (ii) focused ion beam microscopy (FIB) lift-out.

(i) In the Ar ion milling approach. Cross-section samples were prepared by perpendicularly cutting as-polished and as-irradiated surface of ZrN polycrystallines with a Presi diamond cut-off wheel on a Mecatome T180 (Presi, Brié-et-Angonnes, France).The as-polished or as-irradiated surfaces of the cut-off thin plates are glued together like a club sandwich. These samples were thinned to a thickness of ~100 μm through grinding manually on a glass plate using SiC slurry with a particle size of ~5 μm. Further grinding and polishing of the samples were conducted on Ecomet 3 (Buehler, Illinois, USA) with Buehler diamond grinding discs with a grit size of 3 μm. Finally, wedge polishing to a thickness below 100 nm was applied at the central of sandwiched sample, followed by 5 kV Ar ion milling with an 8˚ dual modulation (PIPS II 695, Gatan, USA).

(ii) FIB lift-out TEM samples were prepared using Nova 600 Nanolabs (FEI, USA). Firstly, an electron beam assisted deposition of platinum was applied at a position of interest with a thickness of 0.5 μm, followed by an ion beam assisted deposition of platinum with a thickness of 1.5-2 μm, aiming to reduce gallium ion contamination of the top face of a sample. Following this staircase cuts (25 × 8 × 8 μm) were made on either side of the platinum at 20 nA beam current. The lamina was then cleaned to a thickness of 1-2 μm with successively lower beam currents. At low beam currents (1 nA or less) the

sample was cleaned with a beam angle of +/- 1.5º. Once reduced enough in thickness, the lamina was milled from the bulk material and platinum welded to a micro manipulator. The lamina was then platinum welded to a copper half grid with the probe cut off. The sample was further thinned using a probe current of 100 pA. Typical lamina sizes ranged from 20 x 9 µm to 10 x 5 µm for the width x depth. Samples which were to be analysed with STEM EDS were placed on flag post positions on the grid to limit copper signals on the EDS spectra. The thickness of all finished TEM samples is ~100 nm.

(b) Structure integrity characterisation

BSE imaging and EBSD mapping based on scanning electron microscopy (SEM) were utilized to illustrate the integrity of ZrN after irradiation. The investigation was conducted with a JMS-7800F field emission (JEOL, Tokyo, Japan) equipped with back scatter (BS) detector (SM84030SRBE, Jeol, Tokyo, Japan), EBSD detector, Nordlys Nano (Oxford Instruments, UK) and energy dispersive spectroscopy (EDS) detector, Oxford X-Max 80 (Oxford instruments, UK). BSE images were taken at 10 kV with a probe current of 8 nA and working distance from 3-6 mm. EBSD was conducted at 20 kV with a probe current of 12 nA and working distance of 13 mm and a tilt angle of 70º. 4 x 4 pattern binning and step size of 0.3 µm was used for EBSD mapping. A step size of 0.03 µm was used to map the ion damage layer. EBSD data was processed with Tango processing tools (Oxford Instruments, UK). EDS was conducted simultaneously to the EBSD collection and used to inform the EBSD pattern indexing. The EDS data was subsequently processed with Aztec software (Oxford Instruments, Oxford, UK).

(c) Microstructure and chemical composition characterisation

Microstructure and chemical composition characterisation of the cross-section samples taken from as-polished and as-irradiated materials was performed using a FEI Tecnai F20 G2 S-Twin field emission gun (FEG) scanning TEM (STEM). Additional conventional transmission images, SAD patterns, DF images and HRTEM and high-angle annular dark-field scanning transmission electron microscopy (HAADF-STEM) were acquired with a JEOL JEM 2100F (JEOL, Tokyo, Japan) operated at 200 kV, equipped

with an energy dispersive X-ray (EDX) X-Max 80 mm^2 TLE detector (Oxford Instruments, UK).

X-ray diffraction (XRD) was conducted with Bruker D8 ADVANCE (Bruker, Karlsruhe, Germany) with a Cu K_α source and a LynxEye detector cover. Each sample was scanned from a 2θ of 10º to 80º with a scanning speed of 4˚/min. International Centre for Diffraction (ICDD) cards embedded in the Bruker analysis software were used to identify the sample phases. PeakFit (Systat Software Inc, California, USA) was used to characterise the peak position and FWHM of each peak.

3. Results

3.1. Structure before irradiation

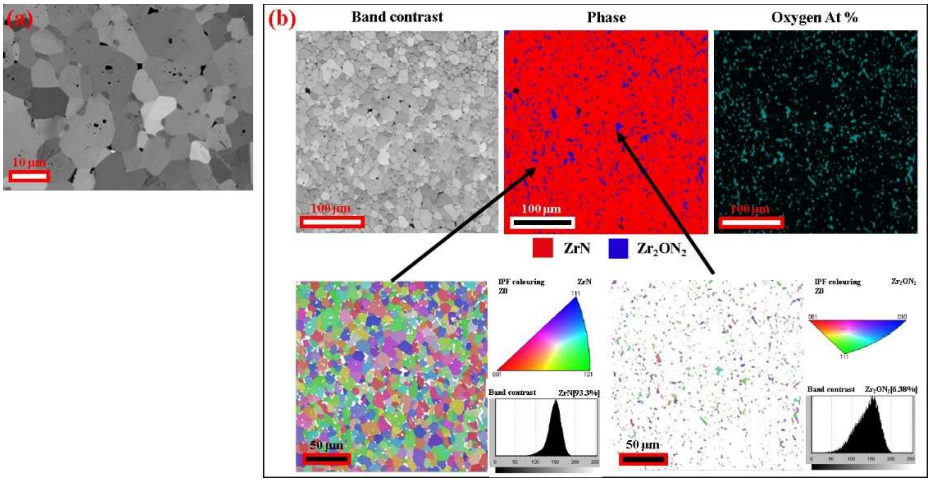

Fig. 1. Microstructure of as-manufactured ZrN polycrystalline. (a) back-scattered electron image; (b) EBSD mapping results including maps of band contrast, phases, oxygen, and crystal orientations of ZrN and Zr_2ON_2 crystallites with their inverse pole figure and band quality included.

The representative microstructure is shown in Fig. 1. The grain structure in the polycrystalline is clearly resolved on an as-polished surface by the lattice channelling contrast, dictated by the crystal orientation of each grain. The variation of channelling effect with crystal orientation gives each grain different yield of backscattered electrons. The higher the yield, the brighter the grain appears, as shown in Fig. 1(a). The dark grains reflect stronger channelling while the white ones have weaker channelling. The grain structure is also resolved using EBSD which has a direct link to the crystal orientation as

well. Fig. 1(b) shows an example EBSD map acquired from the same polished surface. Grain orientation was calculated by identifying patterns with 10º difference to their nearest neighbours. Different colours are used to demonstrate adjacent crystallites having orientation difference of >10º, and the same colour in a continuous region represents same crystal orientation. The grain structure maps in Fig. 1 shows the following characteristics:

(a) The grain boundaries between ZrN grains are either straight or smoothly extended, indicating few, or no secondary particles existing on these boundaries at this resolution level. There are relatively large particles, around 1 μm, existing on grain boundaries or triple junctions. As approved by EBSD, EDS and XRD measurements, these particles were identified as Zr_2ON_2 or a ZrO_2 core with a Zr_2ON_2 shell.

(b) Large pores are found in some triple junctions, these were faceted in shape, relatively small spherical pores were also identified within the ZrN grains.

(c) Twinning was identified in the ZrN matrix.

Through EBSD mapping, we showed that the ZrN polycrystalline consisted of 93.3% ZrN and 6.4% Zr_2ON_2 in the examined region, and the rest can be accounted as voids. The inverse pole Fig. 1(b) shows that neither ZrN crystallites nor Zr_2ON_2 were preferentially orientated. The average grain size is 5.29 ± 3.31 μm and 1.60 ± 0.63 μm for ZrN and Zr_2ON_2 respectively. The numbers of grains analysed, 1195 grains for ZrN and 631 for Zr_2ON_2, should be sufficient to statistically represent the grains inside the as-manufactured polycrystalline. The average aspect ratio was 1.74 ± 0.75, suggesting the ZrN and Zr_2ON_2 grains are close to an equiaxial shape.

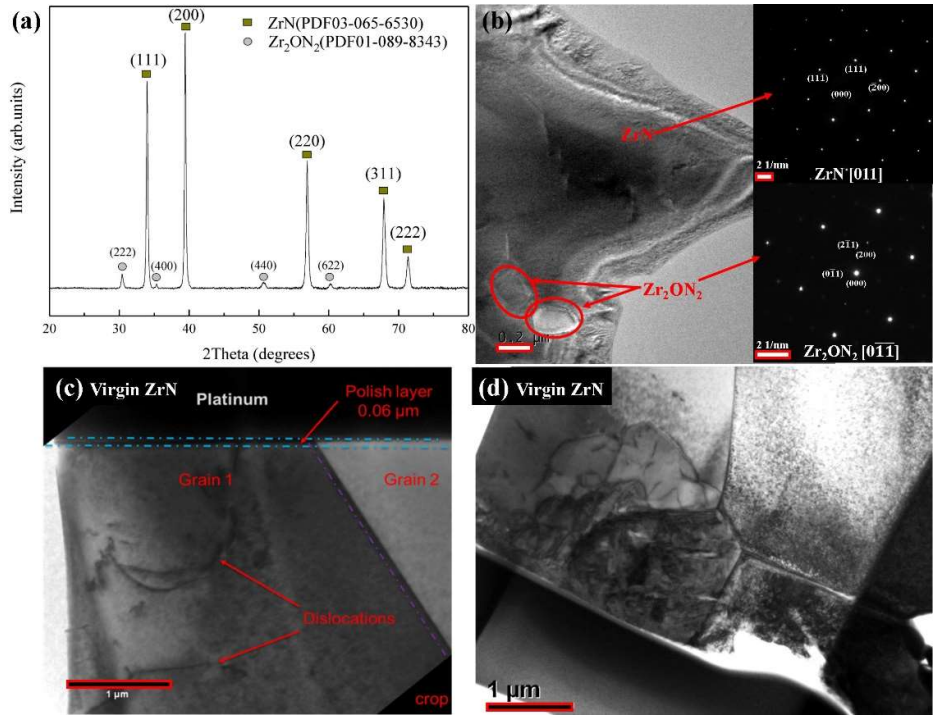

Fig. 2. (a) The XRD patterns acquired on surface of as-manufactured ZrN ceramics; (b) TEM BF image of as-manufactured ZrN and SAD patterns – upper one taken from ZrN grain and lower one from secondary particles embedded inside a ZrN crystal, as circled; (c) cross-section microstructure of as-polished surface before irradiation, showing a thin top-layer (~60 nm) was plastically deformed severely for most of the as-polished surface; (d) occasionally for some grains, a much thicker layer was plastically deformed.

Fig. 2(a) shows the X-ray diffraction pattern of as-manufactured ZrN. There are two sets of diffraction pattern observed. The high intensity peaks represent the diffraction peaks of cubic ZrN, and the one with weak intensity is indexed as cubic Zr_2ON_2. As will be discussed ZrO_2 particles may also have contributed to the intensity of these peaks due to the similar peak positions. The presence of Zr_2ON_2 was not by design and is thought to be a by-product of oxygen contamination in the raw material and/or during hot-pressing.

Fig. 2(b) shows the TEM microstructure of the as-manufactured polycrystalline ZrN. It is noted that inside a ZrN crystallite, there are a few dislocations, which were likely formed during hot pressing. The electron diffraction pattern along [$0\bar{1}1$] zone axis of ZrN grain is presented in the inset of Fig. 2(b), showing the standard cubic structure of ZrN

with an estimated lattice parameter of 4.58 Å. Inside the grain, two smaller particles with a dimension of ~200 nm are identified, as circled by the two red ovals. The SAD patterns along a zone axis of $[0\bar{1}\bar{1}]$ of one of the particles is shown as inset in Fig. 2(b), giving a lattice parameter of 10.19 Å. This value matches the theoretical one 10.1394 Å [15]. The structure of the secondary particle is clearly less packed than ZrN, giving a theoretical density of 5.77 g/cm^3.

Prior to characterising the microstructure of as-irradiated surface, it is necessary to know that of the as-polished one, in order to provide unambiguous comparative study before and after irradiation. Fig. 2(c) shows cross-section TEM images of as-polished surface. The surface was severely deformed with a layer of dislocations developed on top surface with a thickness around tens nanometres for most of the surface. The density of dislocation is too high to have single dislocation resolved clearly. However, in some regions, the dislocation layer is thickened significantly, as shown in Fig. 2(d). The high-density layer on top surface has a thickness of ~200 nm, giving fairly dark contrast in the BF image due to the severe lattice distortion. Going deeper position, dislocation lines are resolved clearly. The depth of plastic deformation introduced by the polish varies with the crystal orientation of each grain relative to the surface. Plastic deformation induced by mechanical finishing is widely noted in other polycrystallines [16].

3.2. Structure integrity after irradiation

The structural integrity of the irradiated layer of the polycrystalline ZrN was assessed with BSE images and EBSD maps. Fig. 3(a) and (b) shows a typical BSE cross-sectional image of an as-polished and as-irradiated surface, respectively. For the as-polished surface, there is no visible contrast variation inside each grain on the surface apart from original features seen inside the bulk material. This is possible since the crystal lattice of the as-polished surface had no changes apart from a thin dislocation layer found on top of the surface, likely too thin to be resolved.

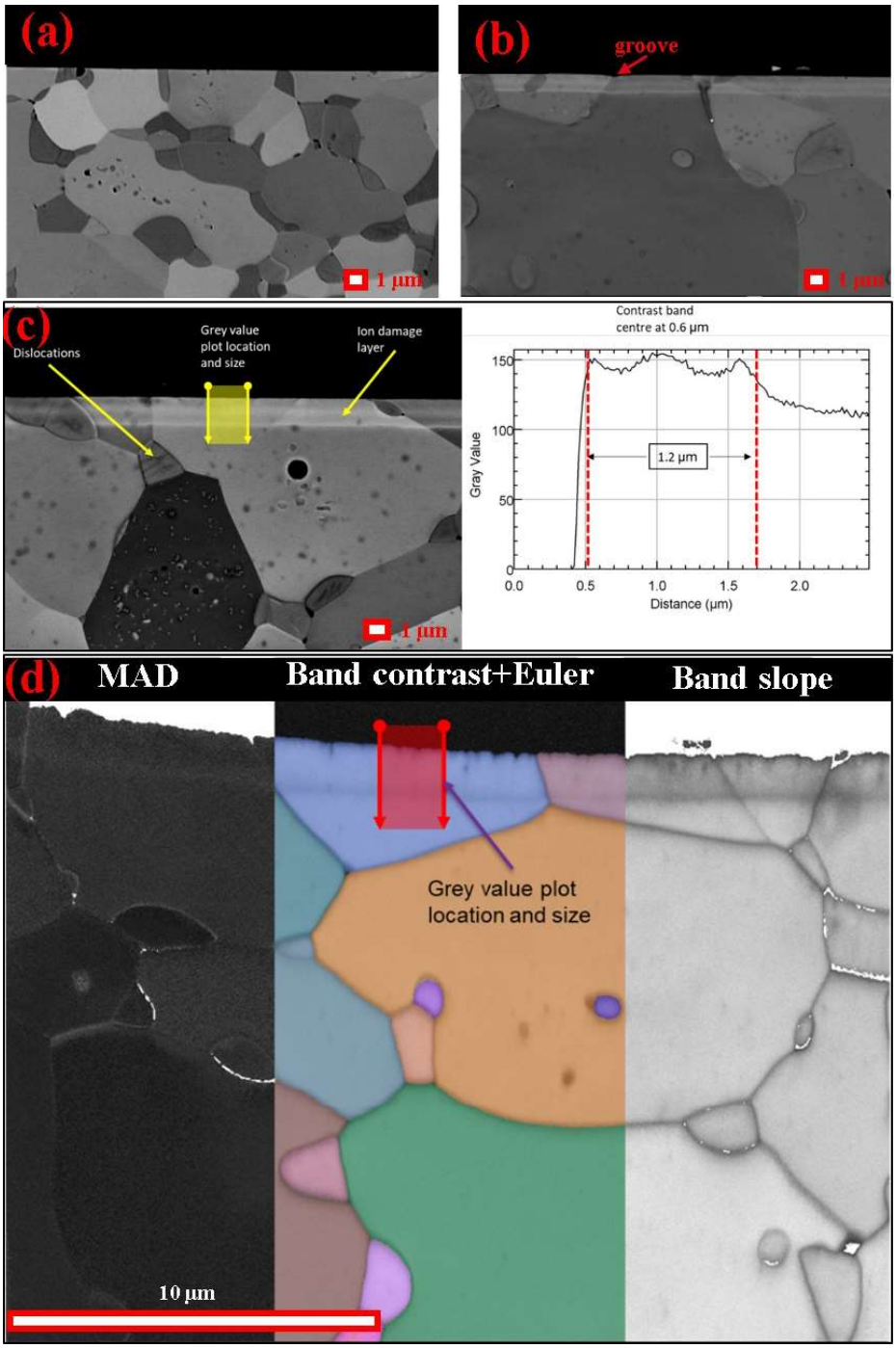

Fig. 3. BSE image of cross-sections of (a) as-polished surface, (b) as-irradiated surface, (c) depth profile of grey value in a ZrN crystallite to distinguish different zones developed by Au ion implantation; (d) EBSD mapping of cross-section of the irradiated surface, including maps of MAD, band contrast with grain orientation and band slope.

For the as-irradiated surface, a layer on the top surface with varied grey contrast was clearly observed, as shown in Fig. 3(b). The front line of this layer, showing higher grey

value, is parallel to the top surface. As the surface is nearly flat, hence the frontline is almost straight. It is noted that, when there is a groove on the surface, the front line sank deeper correspondingly in order to maintain the same depth, as shown at the arrowed position in Fig. 3(b). Overall, the layer had maintained the same depth across the examined region; some fluctuation of the frontline can be seen but in a very small scale. As to be confirmed later, the frontline is the position of irradiation-induced lattice deformation. This observation has demonstrated that regardless crystal orientation, the irradiation damage depth is the same.

Inside influenced layer by irradiation, the following features are noted, as demonstrated by an image with higher magnification in Fig. 3(c):

(a) The grey level of the irradiated layer is improved regardless the crystal orientation of each grain.

(b) Grain boundaries had no visible changes with regard to width, shape and contrast.

(c) Smaller crystallites on the boundaries behaved in the same manner as large ZrN crystallites did.

The EBSD maps produced by pattern quality, expressed as band contrast and band slope, are illustrated in Fig. 3(d). Band contrast and band slope are related to the quality of the Kikuchi patterns produced. The reduction in pattern quality suggests an increase in dislocation density and/or residual strain. Inside the irradiation region, the diffraction band quality has little change apart from a narrow region near the frontline. These maps demonstrate that the irradiation had little change of the crystal structure of ZrN. However, this main structure frame work was heavily distorted around the front plane of irradiation. The mean angular deviation (MAD) is used to indicate the misfit between the measured and the calculated angles between bands, so the larger the MAD value, the higher the misfit and the lower the indexing confidence. It is also a good indicator of lattice strain or defect density. The MAD map shows the irradiation region did have high misfit and lower indexing confidence.

It seems that the structure of grain boundaries between ZrN grains have been well

maintained after irradiation. Both SEM image and EBSD map show no cracking along grain boundaries, or broadening of a grain boundary. This integrity will be further evidenced by the TEM images where one grain boundary inside the irradiation zone has no abnormal features compared to the part in the un-irradiated part, at least at the present level of resolution.

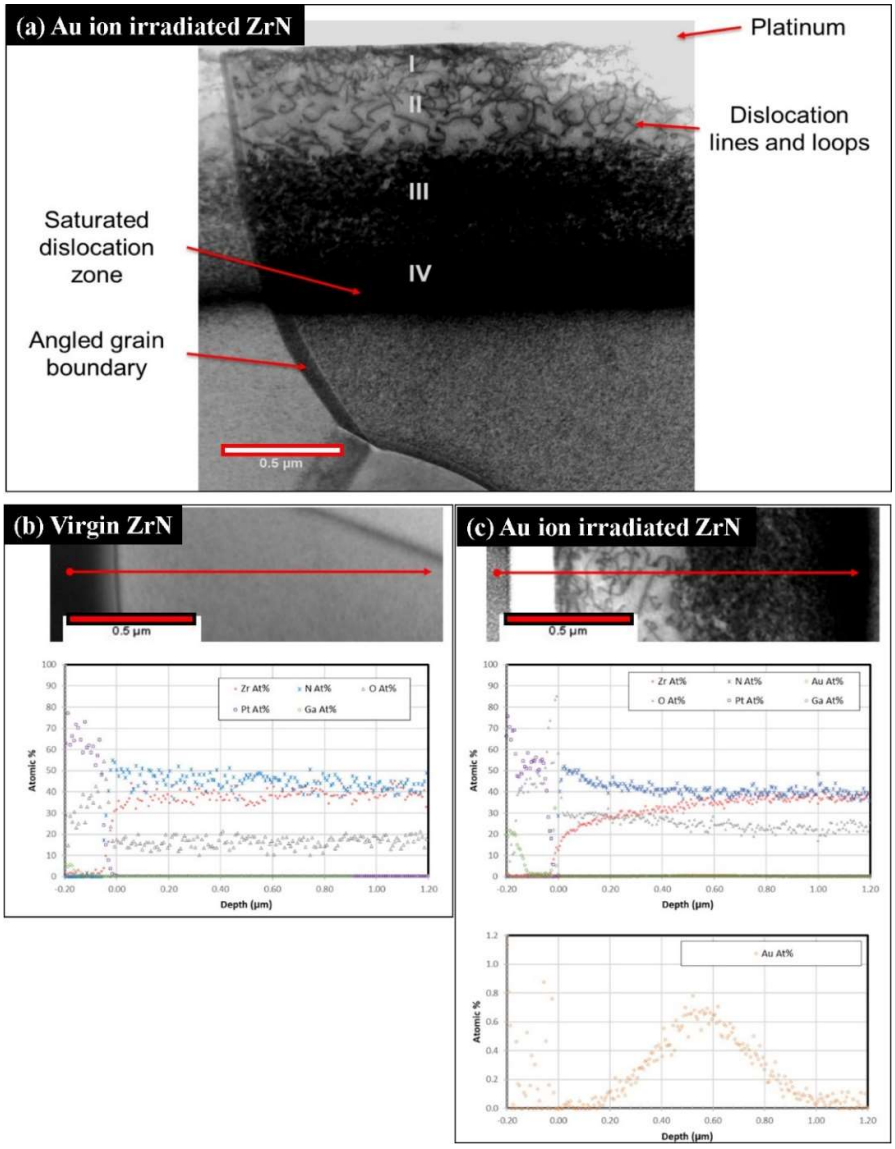

Fig. 4. (a) STEM image (BF) of cross-section of irradiated surface of ZrN polycrystalline (BF). (b-c) Line scan of chemical element starting from an inner position to the top surface of (b) as-polished surface, and (c) as-irradiated surface. A near Gaussian distribution of detected Au content underneath the irradiated surface is shown in (c).

3.3. Structure features and chemical composition after irradiation

(a) Lattice defects

Fig. 4(a) shows the structure features in an irradiated layer of a ZrN crystallite. In this bright field TEM image, the dark contrast ought to come from the distortion of crystal lattice. Based on the lengths of dislocation lines or the intensity of dark region, we can clearly distinguish the irradiated region into four layers, *Layer-I*, *Layer-II*, *Layer-III* and *Layer-IV*, from the top surface into the front plane of ion irradiation zone, as marked in Fig. 4(a). The features in each layer are highlighted as:

- *Layer-I*: The thickness of this layer is 35 ± 1.1 nm, where the dislocations are highly crowded with difficult to resolve each dislocation, but the resolved ones do show that the dislocation lines are fairly long. The estimated dislocation density is 5 x 10^{14} 1/m^2.
- *Layer-II*: The thickness of this layer is about 500 nm, where almost all dislocations can be clearly resolved and have much longer length. The estimated dislocation density is 3.2x10^{14} 1/m^2.
- *Layer-III*: The thickness of this layer is about 500 nm, where dislocations are hardly resolved. However, near the boundary between Layer-II and Layer-III, there are dislocation loops with a diameter of 50 nm can be resolved, and sparsely distributed bright regions can be seen in this region.
- *Layer-IV*: The thickness of this layer is about 200 nm, where no single dislocation can be resolved and the whole region is in dark contrast. However, near the boundary between Layer-IV and the non-irradiated region, dislocation loops are resolved with a diameter of 15 nm.

(b) Chemical composition

To understand the irradiation better, we had a line scan of all chemical elements under STEM mode along a direction normal to the irradiated surface. The results are summarised in Fig. 4(b-c), overviewing chemical elements distribution from an inner position of the sample to its top surface of an as-polished surface (Fig. 4(b)) and as-

irradiated one (Fig. 4(c)). Inside a cross-section of as-polished surface, Zr, N and O were the only 3 elements probed; inside the one of as-irradiated, Au was probed underneath the surface. Pt and Ga were probed in a region just above the surfaces, clearly a consequence of contamination by deposited Pt layer to protect the original surfaces and Ga beam used for lifting TEM samples with FIB.

For the as-polished surface, we have noted that the atomic ratios of Zr/N is close to 1, as a first approximation. However, the fluctuation of the Zr/N ratio tends to bring it to less than 1, and such tendency seems to be reinforced when the position become closer to surface. The lowest ratio is on the surface, with a value of ~2/3. The averaged ratio of Zr/N is 0.86 ± 0.05 along the examined depth of 1.2 μm. O content had almost no variation with position, at a level of 16 ± 2.47 atm%, if the fluctuation is ignored.

For the as-irradiated surface, it is noted that the Zr/N ratio is nearly 1 at position deeper than 0.7 μm, a position close to the middle plane of the Layer-III. From here to the surface, each position shows a gradually reduced Zr/N ratio. The lowest ratio is on the surface, nearly 1/3. The averaged ratio of Zr/N is 0.81 ± 0.17 along the examined depth of 1.2 μm, 0.94 times that on as-polished surface. O content has no change for deeper positions. As the Zr/N ratio starts to increase, the O content also increases steadily from around ~23 to ~30 atm%. The deposited Au were probed in the subsurface, its peaked content in probed at a depth of 0.58 μm with a level of ~0.7 atm%. The detected Au content is close to a near-Gaussian distribution along the deposited depth range with its peak appearing at a depth of 0.58 μm and a FWHM of 0.4 μm.

Due to the absorption by sample and possible contamination, the amount of X-ray generated from light elements cannot be quantified into real content without correction, but the variation trend is not changed when the thickness of the sample is maintained the same. One of the possible contributing factors for the observed reduction of Zr/N ratio on an as-polished surface could be the tapering of the FIB lift-out TEM sample. The thinner thickness gives less absorption of X-ray generated by N, leading to a reduced Zr/N ratio. If we assume all TEM samples had the same thickness and tapering, the much smaller

Zr/N ratio detected on the as-irradiated surface might reflect a truth that Zr/N ratio is reduced by the irradiation. Without further evidences to quantify the Zr/N ratio, we can only conclude that Zr/N ratio might be reduced by the ion irradiation, but there is no evidence to show that Zr/N ration was increased by leaving N vacancies, as claimed by Eageland *et al* [12].

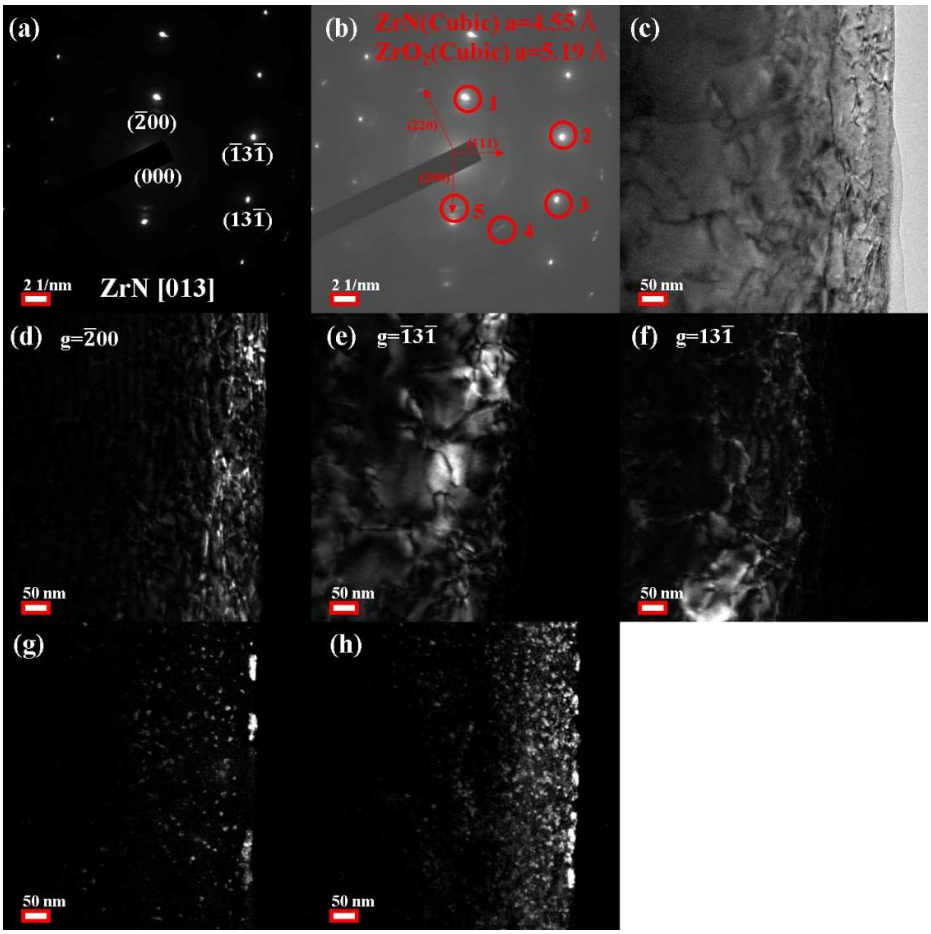

Fig. 5. Diffraction contrast images for characterising lattice defects and small precipitates inside ion irradiated region of ZrN. (a-b) The SAD patterns of irradiated ZrN; (c) BF image; (d-h) DF images with different diffraction spots in sequence.

(c) Structure at nano-metre level

TEM sample prepared by Ar ion milling was thin enough for resolving more structural features at atomic/nano-meter levels. Fig. 5 shows a region near the irradiated surface with a BF (Fig. 5(c)) and a range of DF images (Fig. 5(d-h)). Fig. 5(a) shows the SAD patterns acquired from this region with a zone axis of [013], and three DF images

were recorded with a g of $\bar{2}00$, $\bar{1}3\bar{1}$, $13\bar{1}$ and other extra diffraction spots, as indicated by red circle in Fig. 5(b). The contrast of all defects follows g.**l** > 0, where **l** is the B-W contrast vector, running from the black lobe to that of the white. The defects are very clear in irradiated ZrN from the variation of contrast (Fig. 5(c-h)), and defects are different with different observation points. The dislocation lines and loops can be observed clearly with g=$\bar{1}3\bar{1}$ (Fig. 5(e)), but it is hard to observe any dislocation lines and loops with g=$\bar{2}00$ (Fig. 5(d)). It illustrates that dislocation grows with Burgers vector **b**=$\pm[01\bar{1}]_b/2$ according to the g.**b**=0 invisibility criterion, which is related to the configurational energy [17]. Precipitate-type defects also can be found obviously at depth of ~150 nm (Fig. 5(g-h)), the particles of ~5 nm in size at depth of ~10 nm and smaller ones in the deeper depth. And the nanocrystalline particles are approved as ZrO_2 whose lattice parameters gives a set of diffraction rings matched well by those shown in Fig. 5(b). We can conclude that nanocrystalline ZrO_2 particles precipitated inside the irradiated region.

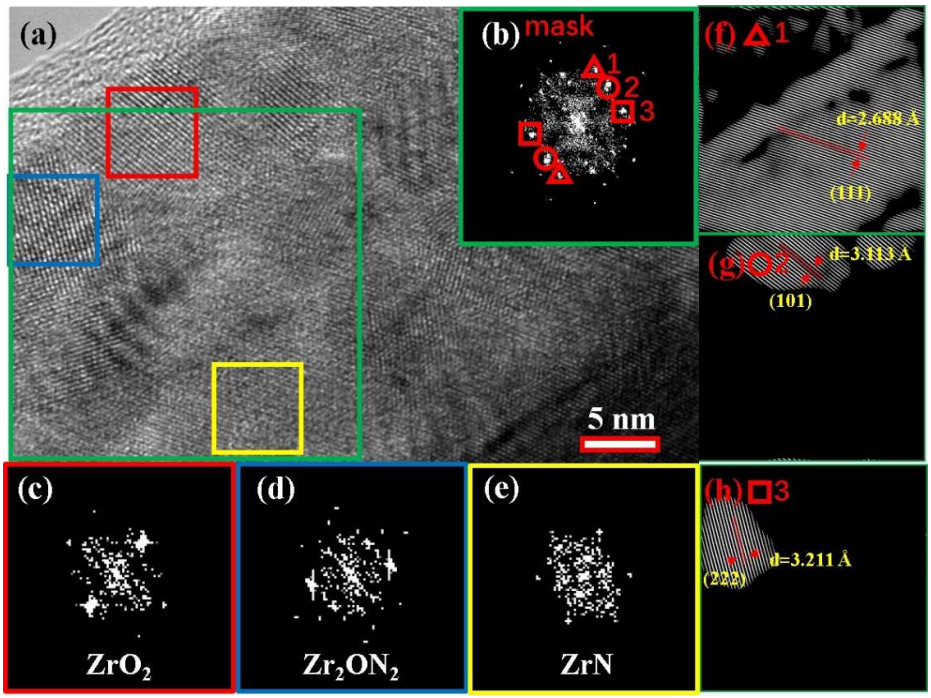

Fig. 6. (a) HRTEM image of irradiated ZrN; (b), (c), (d) and (e) are the FFT patterns of the green, red, blue and yellow squared region respectively shown in (a); (f), (g) and (h) are the inverse FFT patterns of the green area in (a), and twin mask filtering with the red triangle, circle and square in (b) respectively.

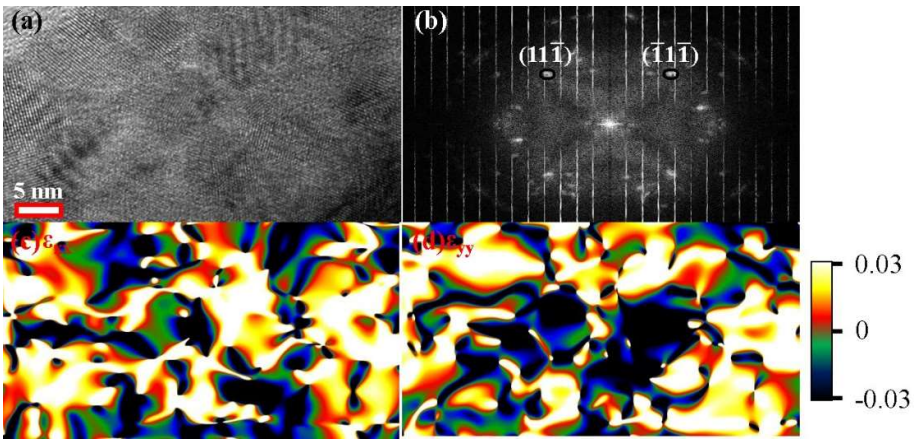

Fig. 7. (a) HRTEM image of irradiated ZrN; (b) The power spectrum of the HRTEM image; Black circles indicate masks used for the geometric phase analysis with g=11$\bar{1}$ and g=$\bar{1}$1$\bar{1}$. (c) and (d) are the corresponding phase images of ε_{xx} and ε_{yy} respectively. The colour scale indicates the displacement as a fraction of the lattice parameter a.

Fig. 6(a) shows the HRTEM image of irradiated ZrN in a region near surface. A layer dispersed with nano-crystallites are clearly shown. There are a lot of nano-crystallites with a size range between ~5 to ~10 nm embedded inside a ZrN crystal. ZrO_2, Zr_2ON_2 and ZrN crystals can be confirmed by the FFT patterns (Fig. 6(c-e)). And it can be seen clearly that the nanocrystalline of ZrO_2 and Zr_2ON_2 in the outermost surface of the grain of ZrN from Fig. 6(f-h). While Au ions impacted the ZrN sample with high speed and energy, the O (oxygen) in the chamber would speed up by Au impacting, then it also impacted the ZrN sample with a certain energy which contribute to the contamination of oxygen. Not only is the lattice constant expanded, but also the polycrystalline exhibits torsion as shown in Fig. 7. Since the lattice strains caused by damage will lead to the image contrast and distortion in HRTEM images, the strain information have been extracted from Fig. 7(a) based on geometric phase analysis (GPA). Fig. 7(c) and Fig. 7(d) show the strain image result along <11$\bar{1}$> and <$\bar{1}$1$\bar{1}$> respectively, while the black regions represent negative strains and white regions show the converse. The variation of strains illustrates that lots of damage exists in irradiated ZrN. It shows that ZrN lattice inside irradiated region is heavily distorted, giving a residual elastic strains up to a level of about 18%. While a particle (neutron, proton or ion) is moving through the lattice at high velocity, it will slow as a result of momentum transfer, coulomb interaction and electron

interaction forces. Thus the structure of lattice is modified resulting in a high level of lattice disorder. Nano crystallinity is easily generated by the torsional effects of the impinging fast heavy ions (or neutrons / protons).

4. Discussion

Our results clearly show that 4 MeV Au ions with a fluence up to $5x10^{16}/cm^2$, did not destroy the crystal lattice framework of ZrN, and the primary microstructure of its polycrystalline as well. This observation has further approved the excellent resilience of ZrN crystal to ion irradiation without amorphization observed, even after irradiating by a much higher fluence than those used in previous studies [10, 12, 14]. The outstanding integrity of its polycrystalline, manufactured through a traditional ceramic processing route, is of particular importance in developing IMF for transmuting transuranium elements [3]. Apart from the merits of one's main interest in ZrN polycrystalline, we did observe the following structural and chemical features inside the irradiated layer, as evidenced in Fig. 3-6 with details, which may evidence our understanding of the possible irradiation process, or provide structural information for other interests in research and application:

(i) Most of Au ions were deposited beyond the long dislocation layer, and ZrN lattice is heavily distorted by dislocation loops and elastic strains

(ii) ZrO_2 or Zr_2ON_2 crystallites with a diameter of ~5 nm were developed inside the top layer of the irradiated regime.

(iii) The nitrogen/oxygen content increased and zirconium reduced in the top layer of the irradiated regime.

(iv) Inside the top layer of irradiated regime, long dislocations with a density of $3.2x10^{14}$ $1/m^2$ were developed.

(v) Beyond the Au ion enriched layer, the ZrN lattice is also heavily distorted by dislocation loops and elastic strains.

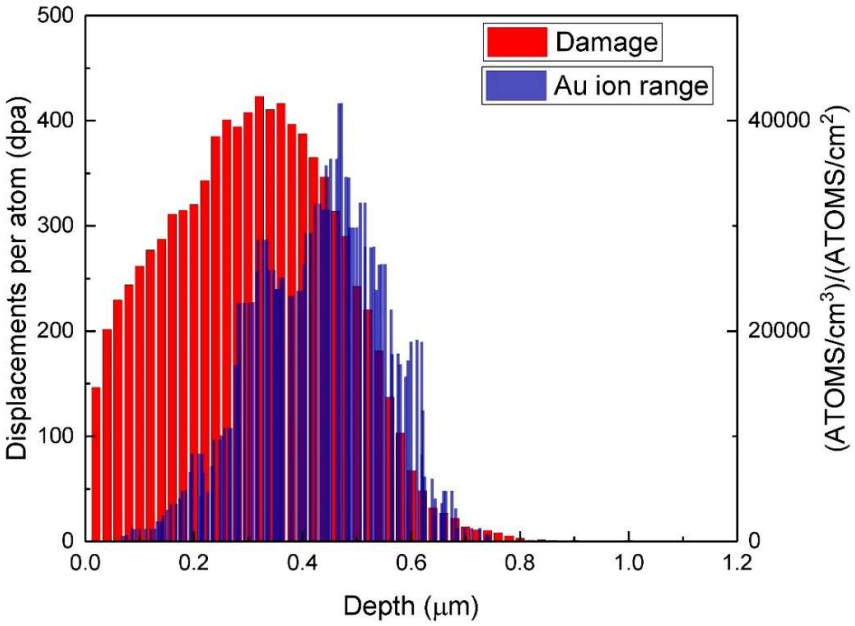

Fig. 8. Lattice damage and Au ion deposition profile estimated with SRIM in ZrN irradiated by 4 MeV Au ions with an accumulated fluence of $5x10^{16}/cm^2$.

For the implantation of Au ions, we can estimate its deposition profile using the classic SRIM [18] with an average threshold displacement energy (E_d) of 40 eV for both zirconium (Zr) and nitrogen (N) atoms [12, 19]. Note, the values of E_d for Zr is based on estimated values of ZrC, while the E_d for N is unknown, hence assumed to be the same as Zr based on the sublattice structure [20]. The results are shown in Fig. 8, where blue bars describe the histogram profile of deposited Au underneath the surface. The profile is close to a Gaussian distribution, and fitting shows the central position is at a depth of 0.5 μm, and FWHM of 0.31 μm. The central positions of the Gaussian distribution are very close between those of measured (0.58 μm) and estimated. However, the estimated FWHM is about 22.5% smaller than the measured one. Such inconsistence ought to be associated to the assumptions of E_d, but as a first approximation, this assumption should be good enough to estimate the Au deposition inside ZrN. In addition, the contamination of oxygen may have impact on the estimation of SRIM.

Without considering the thermal effect, the predicted damage region should be inside about 0.5 μm. Our investigation shows that inside this region, only long dislocations are seen in Layer-I and Layer-II with crystal structure of ZrN well maintained and no any

amorphous phase developed. We believe that thermal-induced recovery must be responsible for the observed. With thermal effect considered, we might be able to explain other structural features seen inside the irradiated layer, as detailed below.

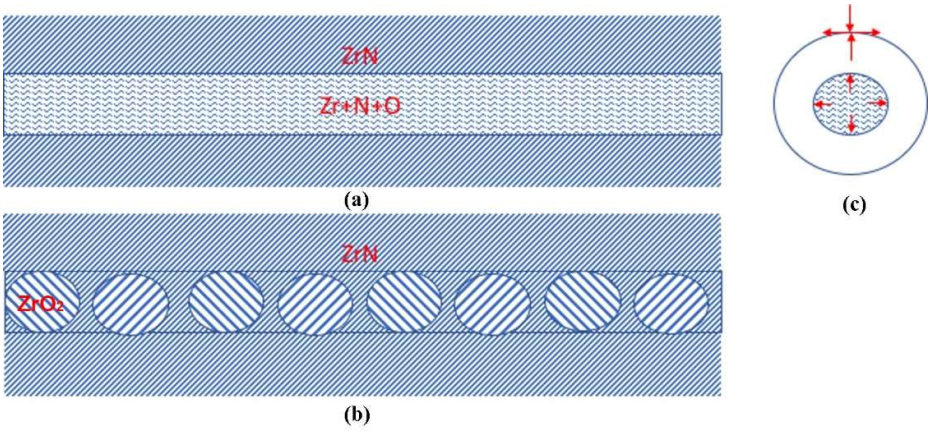

Fig. 9. Schematics showing a ion trajectory composed of a mixture of Zr, N and O that are excited by the thermal spike and Coulomb explosion, as shown in (a), followed by crystallisation or recrystallization leading to the formation of spherical ZrO_2 particles and epitaxial ZrN crystal formed inside the track, as shown in (b). When the ion track is formed, the transient volume expansion leave the track itself under hydrostatic pressure and surroundings under shock stress wave with shear stress developed by the tension along the hoop directions and compression along the radial directions, as shown in (c).

In general, passing through a solid material, a energetic heavy ion is expected to lose its energy via two independent mechanisms: electronic excitation/ionization (also called Coulomb explosion) [18], and elastic collisions with the nuclei of the target atoms. High energy heavy ion irradiation can lead to high density of electronic excitation in materials along its pathway, and this is a primary mechanism for a passing ion to lose its energy. On the other hand, energy loss by the elastic collisions with the nuclei of the target atoms is so small that it is normally ignored in discussion. Hence, the energy loss along a trajectory of a heavy ion leads to a very local and high excitation of atoms in the lattice through ionization, making atoms around the heavy ion pathway very different in structure and possibly in chemistry from the parent solid. This coulomb is hence formed as a trajectory that are different from the parental solid. The thermal spike and Coulomb explosion models are frequently used to describe what might happen inside the heavy ion track. It is generally agreed that the following could appear inside the trajectory: The

density of atoms is reduced in the core and a surrounding region is densified. Such an unstable system is likely rebalanced by recrystallization, amorphization or even phase transformation, depending on the physical and chemical properties of the target material. Hence, after irradiation, the ion trajectory may not be marked by amorphous phase, but could be a recrystallized region, or a region with different phases.

Based on the aforementioned physical process of energetic heavy ion irradiation, the detected chemical composition and crystal structure inside the irradiated regime, we assume that ion trajectory has a chemical composition of Zr, N and O. During irradiation these atoms are likely exited to a highly disordered structure, or even to a molten state. Upon cooling, recrystallization or precipitation occurs when enough thermal conditions are provided for the kinetic to proceed; otherwise an amorphous track would have been seen. The speculated ion trajectory and its change are schematically shown in Fig. 9.

Following this hypothesis, if there are enough oxygen atoms inside the ion trajectory, the size of the zirconia crystallites or diameter of ZrN should be the same as the diameter of the ion trajectory cylinder. As ZrN could precipitate through an epitaxy process to minimize interface energy, we may not be able to differentiate the precipitated ZrN from the parental ZrN, which is true as shown in Fig. 9. However, we can identify the ZrO_2 crystallites without ambiguity. The measured average diameter of ZrO_2 crystallites is ~5 nm, a size very close to the measured ion trajectory channel by Khalil *et al* who measured a diameter of ~5 nm for Au ion trajectory in InP [21].

Based on this model shown in Fig. 9, the expansion of the trajectory applies a shock stress wave through its fast expansion. The stress wave applied to the surrounding ZrN crystals leads to compression along radial directions and tension along hoop directions, together resulting in a maximum shear stress along 45º deviated from the radial direction. We believe that it is this shear stress that drives the initiation and gliding of dislocations. Inside the inelastic impact region, the region near the ion trajectory gives highest possible temperature, as shown in Fig. 9(a), which leads to a lowest possible critical shear stress for a dislocation to glide. At the same time, this is the region that highest possible shear

stress can appear, as both the tensile along hoop direction and compression along radial direction decline at positions away from the trajectory boundaries. Altogether, dislocations in a region around a trajectory can glide easily, giving very long dislocation lines and lower dislocation density as the density is governed by critical shear stress.

When the position goes deeper than the peak position of deposited Au ions (>0.58 μm), there are no long length dislocation lines, apart from dislocation loops. We believe that this is a consequence of no more inelastic collision exists between Au ions and atoms in ZrN in this region, and hence much lower transient temperature and shear stress exist, making dislocation loops difficult to glide for long length dislocation development. Because of the higher gliding resistance, it is therefore expected to see much higher dislocation density in this region, which is well evidenced in Fig. 4 where the density of dislocation loops is too high to be resolved in the TEM image.

In the near top surface region, the pre-existing dislocation on the polished surface might have provide extra resistance for dislocation glide, hence higher density dislocation with relative shorter length is observed.

5. Conclusions

BSE images and EBSD maps show that, after irradiated by 4 MeV Au ions with a total fluence of $5x10^{16}/cm^2$, the structure integrity of the polycrystalline ZrN is well maintained with no crystal structure change of ZrN as the primary phase and Zr_2ON_2/ZrO_2 as the secondary. The characterisation in this study has provided direct evidence that ZrN polycrystalline, manufactured via typical ceramic processing route, can be used for advanced nuclear fuel design.

The crystal orientation of ZrN grains in the polycrystalline has no influence on the implantation of Au ions and their damage at lattice level. Au ions are deposited underneath the surface, showing a symmetric Gaussian distribution profile with peak position at 0.58 μm away from the surface and a full width at half maximum of 0.4 μm, which is close to the prediction by SRIM when the average threshold displacement energy (E_d) of 40 eV is set for both zirconium and nitrogen (N) atoms. Whether there is a

preferential sputtering between Zr and N is not conclusive and further study is needed.

Development of lattice defects and recrystallization do appear inside the irradiated region. The irradiated region is composed of four layers, including long dislocation line region with relatively lower density near the surface (Layer-I and Layer-II) and dislocation dipoles with high density (layer-III and Layer-IV). Discrete ZrO_2 crystallite with a diameter of ~5 nm are developed and dispersed inside ZrN crystals likely through recrystallization during ionisation as Au ion passing through the irradiated layer. Based on geometric phase analysis, ZrN lattice inside irradiated region is heavily distorted, giving a residual elastic strains up to a level of about 18%.

Acknowledgments

The present work was financially supported by the National Natural Science Foundation of China (51532009, 51502322, 11575275), Science and Technology Commission of Shanghai Municipality (16DZ2260603), Shanghai Technical Platform for Testing and Characterization on Inorganic Materials (14DZ2292900), and Loughborough University's PhD studentship provided to SR. The authors acknowledge use of facilities within the Loughborough Materials Characterisation Centre.

References

[1] D.J. Hill, Nuclear energy for the future, Nature Mater. 7 (2008) 680-682.

[2] D.E. Beller, G.J.V. Tuyle, D. Bennett, G. Lawrence, K. Thomas, K. Pasamehmetoglu, N. Li, D. Hill, J. Laidler, P. Fink, The U.S. accelerator transmutation of waste program, Nucl. Instrum. Methods Phys. Res., Sect. A. 463 (2001) 468-486.

[3] Y.W. Lee, H.S. Kim, S.H. Kim, C.Y. Joung, S.H. Na, G. Ledergerber, P. Heimgartner, M. Pouchon, M. Burghartz, Preparation of simulated inert matrix fuel with different powders by dry milling method, J. Nucl. Mater. 274 (1999) 7-14.

[4] K. Wheeler, P. Peralta, M. Parra, K. Mcclellan, J. Dunwoody, G. Egeland, Effect of sintering conditions on the microstructure and mechanical properties of ZrN as a surrogate for actinide nitride fuels, J. Nucl. Mater. 366 (2007) 306-316.

[5] Y. Tang, G.J. Zhang, J.X. Xue, X.G. Wang, C.M. Xu, X. Huang, Densification

and mechanical properties of hot-pressed ZrN ceramics doped with Zr or Ti, J. Eur. Ceram. Soc. 33 (2013) 1363-1371.

[6] M. Streit, F. Ingold, M. Pouchon, L.J. Gauckler, J.P. Ottaviani, Zirconium nitride as inert matrix for fast systems, J. Nucl. Mater. 319 (2003) 51-58.

[7] M. Streit, F. Ingold, Nitrides as a nuclear fuel option, J. Eur. Ceram. Soc. 25 (2005) 2687-2692.

[8] M.K. Meyer, R. Fielding, J. Gan, Fuel development for gas-cooled fast reactors, J. Nucl. Mater. 371 (2007) 281-287.

[9] L. Gribaudo, D. Arias, J. Abriata, The N-Zr (Nitrogen-Zirconium) System, J. Phase Equilib. 15 (1994) 441-449.

[10]Y. Yang, C.A. Dickerson, T.R. Allen, Radiation stability of ZrN under 2.6MeV proton irradiation, J. Nucl. Mater. 392 (2009) 200-205.

[11]J. Gan, Y. Yang, C. Dickson, T. Allen, Proton irradiation study of GFR candidate ceramics, J. Nucl. Mater. 389 (2009) 317-325.

[12]G.W. Egeland, J.A. Valdez, S.A. Maloy, K.J. Mcclellan, K.E. Sickafus, G.M. Bond, Heavy-ion irradiation defect accumulation in ZrN characterized by TEM, GIXRD, nanoindentation, and helium desorption, J. Nucl. Mater. 435 (2013) 77–87.

[13]A.I. Ogarkov, S.V. Shevtsov, K.B. Kuznetsov, I.A. Kovalev, A.S. Chernyavskii, K.A. Solntsev, Irradiation of titanium, zirconium, and hafnium nitrides with high-energy ions, Inorg. Mater. 52 (2016) 561-565.

[14]K.B. Kuznetsov, I.A. Kovalev, A.N. Nechaev, A.I. Ogarkov, S.V. Shevtsov, A.S. Chernyavskii, K.A. Solntsev, Stability of the structure of compact zirconium nitride ceramics to irradiation with high-energy xenon ions, Inorg. Mater. 52 (2016) 1235-1239.

[15]S.J. Clarke, C.W. Michie, M.J. Rosseinsky, Structure of Zr 2ON 2 by Neutron Powder Diffraction: The Absence of Nitride-Oxide Ordering, J. Solid State Chem. 146 (1999) 399-405.

[16]J. Wade, P. Claydon, H. Wu, Plastic Deformation and Cracking Resistance of SiC Ceramics Measured by Indentation, Ceram. Eng. Sci. Proc. 35 (2014) 91-100.

[17]P. Li, J.M. Howe, Dislocation reactions in ZrN, Acta Mater. 50 (2002) 4231-4239.

[18]J.F. Ziegler, J.P. Biersack, M.D. Ziegler, The Stopping and Range of Ions in Matter, fifth ed., Springer, New York, 2008.

[19]G.S. Randhawa, H.S. Virk, Stopping power and range of heavy ions in solids: A comparative study, Radiat. Meas. 26 (1996) 541-560.

[20]S. Pellegrino, L. Thomé, A. Debelle, S. Miro, P. Trocellier, Radiation effects in carbides: TiC and ZrC versus SiC, Nucl. Instrum. Methods Phys. Res., Sect. B. 327 (2014) 103-107.

[21]A.S. Khalil, L.T. Chadderton, A.M. Stewart, M.C. Ridgway, D.J. Llewellyn, A.P. Byrne, Track formation and surface evolution in indium phosphide irradiated by swift heavy ions, Radiat. Meas. 40 (2005) 770-774.